Electrical characteristics of a Hall effect thruster body in a vacuum facility testing environment

Jonathan Walker[1], Dan Lev[1*], Mitchell L. R. Walker[1], Vadim Khayms[2] and David King[3]

*Correspondence:
dan.lev@gatech.edu

[1] High-Power Electric Propulsion Laboratory (HPEPL), Georgia Institute of Technology, Atlanta, GA 30332, USA
[2] Lockheed Martin Space Systems Company, 1111 Lockheed Martin Way, Sunnyvale, CA 94089, USA
[3] Formerly Space Exploration Technologies Corporation, 18390 NE 68th St, Redmond, WA 98052, USA

Abstract

The operational characteristics of Hall effect thrusters are altered by conductive surfaces in vacuum facilities. Conductive surfaces alter charge distribution in the plume by providing pathways for electron-ion recombination that do not exist in the spaceflight environment. Charge recombination pathways impact thruster performance and plume behavior through mechanisms that are not entirely understood. The incomplete understanding of the relationship between charge recombination pathways and thruster behavior limits the ability to characterize thruster performance through ground testing. This paper quantifies the effect of polarity and magnitude of body-to-cathode voltage on coupling between the thruster body and the local plasma environment. The effort operates the T-140 Hall thruster at a single, fixed operating condition of 300V, 3.5 kW, with anode and cathode xenon flow rates of 11.6 ± 0.03 mg/s and 1.61 ± 0.12 mg/s, respectively. During data collection, the chamber was maintained at a pressure of 8.7×10^{-6} Torr-Xe. The thruster body-to-ground voltage is manipulated by varying body-to-ground resistance. Results show the thruster pole face and body circumference couple to the local plasma environment through distinct sheaths. The polarity of the body-to-cathode voltage determines the characteristics of these sheaths. Therefore, the body-to-cathode voltage controls the interaction between the thruster body recombination pathway and the local plasma environment.

Keywords: Electric Propulsion, Hall Thrusters, Facility Effects, Electrical Effects, Plasma-Surface Interaction

Introduction

In the flight environment, Hall effect thrusters (HETs) produce a beam of ionized propellant and neutralizing electrons that propagate indefinitely into the vacuum of space. To best duplicate the space environment in ground test facilities, HETs are tested in vacuum chambers with the lowest achievable pressures to minimize pressure effects on thruster performance [1–4]. However, the mean free path of energetic ions produced in HETs is well above the size of even the largest test facilities [5]. Therefore,

the conductive surfaces of a chamber provide an artificial path for ions and electrons in the plume to recombine.

Previous studies conducted at the Georgia Institute of Technology High Power Electric Propulsion Laboratory (HPEPL) focus on identifying and characterizing these charge recombination pathways [6–11]. Results from these studies demonstrate that both the body of a HET and conductive surfaces in the test facility serve as recombination pathways for the neutralization of ions produced by the thruster. The vacuum facility and thruster body become elements of the discharge circuit as plasma produced by the thruster electrically couples to conductive surfaces in the chamber. The impedance of these charge recombination pathways has capacitive, inductive, and resistive contributions as with any real element in an electrical circuit. Figure 1 shows a graphical depiction of the recombination pathways.

In the flight environment, the chamber recombination pathway is absent, and the thruster body and plume recombination pathways behave differently due to a reduction in neutral background gas found in test facilities [9]. The addition of these artificial circuit elements modifies electrical potential at nodes and alters the dynamic behavior of the circuit. Moreover, the impact of electrical coupling on thruster behavior is unique for each test facility and thruster combination. There is a need to characterize the correlation between artificial recombination pathways present in the test environment and thruster behavior with the long-term goal of developing recommended practices to mitigate the impact of artificial recombination pathways on measurements taken in the test environment.

To this end, preceding research at HPEPL has focused on characterizing the impact of artificial recombination pathways on thruster behavior by controlling the degree of coupling between the thruster and the facility. Three independent variables were identified to control the degree of facility coupling: cathode position, chamber potential via plume witness plate biasing, and thruster body potential.

This manuscript examines the thruster body potential in greater detail than considered in [6–9]. Previous studies examined free parameters with the thruster body
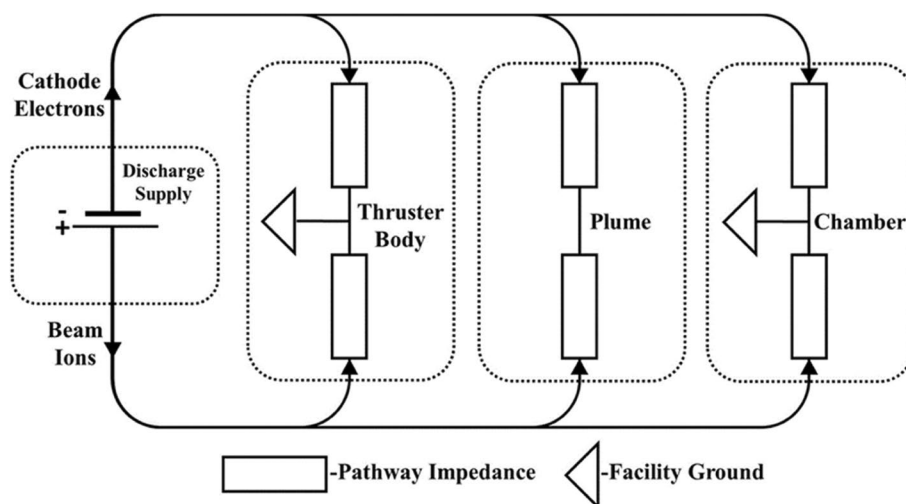

Fig. 1 Typical charge recombination pathways in the test facility

tied to the facility ground or floating. Peterson [12] electrically floated and biased the HERMeS 12.5-kW Hall thruster to cathode or ground potentials. He showed that the thruster body conducted over 13% of the discharge current when the thruster was grounded and with exposed conducting front poles, while insulating the front poles led to a collected current of less than 4% with a cathode-tied electrical configuration. Peterson also showed that when electrically floating the thruster body, its potential can be as low as $-45\,\text{V}$ below ground with conducting front poles. He concluded that several possible electron and ion pathways exist for each thruster body electrical configuration and that the pathways may also influence the ionization region and discharge stability in the thruster. McDonald [13] grounded and electrically floated the H6 HET body with exposed conducting front pole pieces. He showed that more than 10% of the discharge current might be conducted through the thruster body. McDonald postulated that the main current-driving mechanism is through electrons impinging upon surfaces on the thruster body, adjacent floating or grounded surfaces, and the chamber wall. Katz et al. [14] described the possible recombination pathways of electrons and ions in the space environment onboard satellites. He showed that insulating surfaces on the thruster body greatly reduces the collected electron current ($3\,\text{mA}$ of $20\,\text{A}$). In comparison, this value goes up by two orders of magnitude when the conducting surfaces are exposed ($300\,\text{mA}$ of $20\,\text{A}$). Katz also showed that as the thruster body potential is increased closer to ground potential, the current collected by the thruster body increases almost exponentially. Katz argued that when the thruster body is floating, electrons are repelled by the sheath potential forming on the thruster body in order to equalize their current density to that of the ion saturation current. At the same time, biasing the thruster body to cathode or ground potentials reduces the repelling sheath voltages and allows the electrons to close a circuit loop by impinging on different thruster surfaces depending on the local electron temperature. Watanabe [15] measured the floating potential of a high-voltage 2-kW HET and showed that the floating-to-ground voltage decreased sharply with an increase in the discharge voltage, from $-22\,\text{V}$ (at $300\,\text{V}$) to $-75\,\text{V}$ (at $800\,\text{V}$). Watanabe postulated that at high discharge voltages, the local electron temperature close to the thruster surface increases, thus driving down the thruster body floating potential to very low values. Consequently, and to minimize the energy of the ions impinging on the thruster body, he decided to bias the thruster body to cathode potential. Lastly, using the H6MS Hall thruster Hofer [16] demonstrated that there is little impact of the thruster electrical configuration on the overall discharge current.

In order to characterize the relationship between body potential, thruster behavior, and facility coupling, a methodology is needed to manipulate thruster body voltage relative to facility ground and plasma potential. The floating HET body in a test facility self-biases to a potential of approximately $-30\,\text{V}$ in response to the local plasma environment near the thruster [6, 7]. By adjusting the resistance between the thruster body and ground, the thruster body potential can be varied between the fully isolated configuration and facility ground. This configuration allows the test environment to duplicate some of the characteristics of the flight environment. Of significant interest in this study is examining the change in polarity of the body-to-cathode voltage as the thruster body is allowed to float above the cathode voltage. Data from the SMART-1 mission indicate

that positive body-to-cathode voltages have a significant impact on the behavior of the discharge circuit [17, 18].

Design of Experiment

Test facility

All experiments were conducted in Vacuum Test Facility 2 (VTF-2) at the HPEPL. VTF-2 is a stainless-steel chamber with a diameter of 4.9 m and a length of 9.2 m. Rough vacuum is achieved using a 495 ft³/min rotary vane pump and a 3800 ft³/min blower. High vacuum is achieved using ten liquid nitrogen cooled CVI TM1200i cryopumps connected to two Stirling Cryogenics SPC-4 compressors [19]. The system provides a combined xenon pumping speed of 350,000 l/s and achieves a base pressure of 1.9×10^{-9} Torr. The pressure is monitored using two Agilent Bayard-Alpert (BA) 571 hot-filament ionization gauges. One ionization gauge is mounted to a flange on the chamber exterior, and the second gauge is mounted 0.3 m downstream of the thruster exit plane and 0.6 m from the thruster centerline. During testing, nominal operating pressures were 1.3×10^{-5} Torr-Xe at the external gauge and 8.7×10^{-6} Torr-Xe at the internal gauge. The reported pressures are corrected for xenon using Eq. (1):

$$P_c = \frac{P_i - P_b}{2.87} + P_b \tag{1}$$

where P_c is the corrected pressure, P_b is the base pressure, P_i is the indicated pressure, and 2.87 is a gas specific correction constant.

Hall effect thruster

The experiments detailed in this work were performed using a T-140 HET developed through a collaboration between Space Power Inc., Keldysh Research Center, and Marconi Space [20]. The T-140 features a channel manufactured from M26-grade boron nitride with an outer diameter of 143 mm and a width of 23 mm. The magnetic coils are coaxial with the discharge channel; therefore, the magnetic field lacks an external separatrix. An EPL HCPEE 500 hollow cathode was positioned 2.5 cm downstream
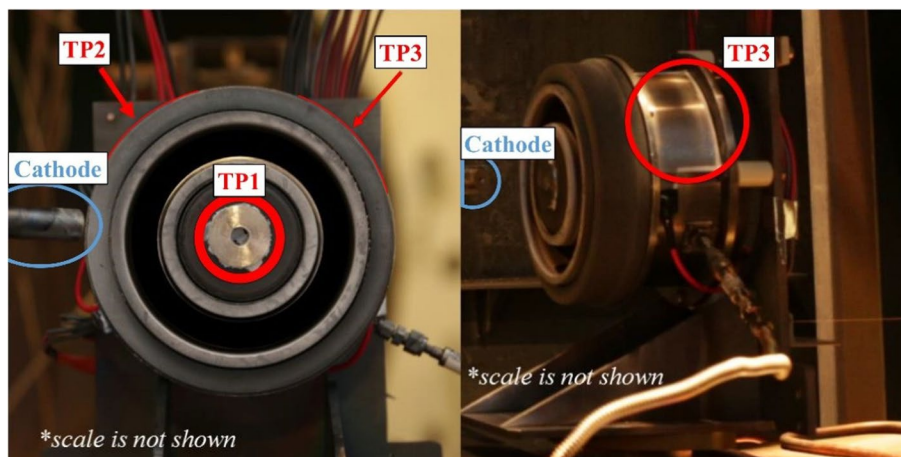

Fig. 2 T-140 three witness plates and cathode position

of the T-140 exit plane and 18.5 cm from the centerline. Figure 2 shows the cathode is inclined at 55° with the orifice directed towards the channel. Ultra-high purity grade 5 xenon was used for running both the thruster and the cathode. Anode and cathode flow rates were controlled with separate MKS 1179A mass flow controllers. The flow rates for the anode and cathode were 1.61 ± 0.12 mg/s and 11.6 ± 0.03 mg/s, respectively. The T-140 was operated at 300 V and discharge power of 3.5 kW for all tests. The thruster was operated for 2 h before data collection to reach thermal equilibrium and allow for the removal of channel surface contaminants [21].

Witness plate configuration

Three witness plates are fixed to the surface of the thruster body with electrically isolating materials to investigate current collection in different regions of the plasma environment near the T-140. Figure 2 shows the position of the plates on the thruster.

TP1

TP1 is an annular witness plate manufactured from 316 stainless steel for thermal considerations and positioned to measure current from the face of the thruster inner front pole piece. The plate stock has a thickness of 0.159 cm, with annular dimensions of 9.67-cm OD and 2.59-cm ID. The inner pole piece of the T-140 features mounting screws exposed to the local plasma environment in a region of bulk ion production that exists due to charge exchange collisions [22, 23]. Therefore, the plate is expected to receive a net ion flux. There is interest in investigating current collection in this region due to ion bombardment and erosion that can be a life-limiting mechanism with specific thruster designs [24, 25]. The body-facing side of TP1 is electrically isolated using Aremco Ceramadip and bonded to the inner magnetic pole with Aremco Ceramabond. Electrical resistance to the thruster chassis was measured with a Fluke 87 V digital multimeter to be 20 MΩ. The electrical connection was made with 14-AWG silicone jacketed wire running through the center hole of the T-140 pole piece.

TP2 and TP3

The TP2 and TP3 witness plates are positioned on regions of the outer circumference of the thruster body, where the magnetic field is expected to intersect the surface. Because magnetic fields are solenoidal, the magnetic field of a HET extends beyond the front pole face and must intersect the thruster body to reconnect with the pole piece. In this region, the magnetic field strength is adequate to confine electron drift along magnetic field lines, and the plates are expected to receive a net electron flux [6, 26]. Since the T-140 features an externally-mounted cathode, TP2 is positioned on the cathode-facing side of the body, and TP3 is positioned on the opposing side. TP2 and TP3 are manufactured from an aluminum plate with a thickness of 0.159 cm and dimensions of 5.08 cm by 10.16 cm. The body-facing sides of TP2 and TP3 are electrically isolated using Aremco Ceramadip, but the plates are adhered with Red RTV acid cured silicone instead of Ceramabond due to lower operating temperatures in this region. Electrical resistance

Walker *et al. Journal of Electric Propulsion*   (2022) 1:18

Page 6 of 24

to the HET chassis was measured with a Fluke 87 V digital multimeter to be 20 MΩ. The electrical connection was made with 14-AWG silicone jacketed wire insulated with self-vulcanizing silicone tape.

Control of thruster body potential

Previous work shows that the T-140 body floats to a potential of approximately −30 V when electrically isolated from the electrical ground [6, 7]. By varying the resistance between the T-140 body and ground, the potential of the body can be adjusted between −30 V and ground. Two 50-W, 25-Ω ceramic resistors are used for this purpose. Figure 3 presents a schematic of the electrical configuration. The T-140 body and witness plates are connected to the resistor and ground in a star configuration to minimize the formation of ground loops.

It is important to note that the potential of reference reported in this study is the thruster body to cathode potential. We chose this as the cathode potential conventionally serves as the common potential to the electrical circuit of the electric thruster. The cathode tends to establish negative voltage with respect to ground potential, as discussed in this article.

Diagnostics

Results presented in this article focus on current and voltage data collected using a pair of Teledyne Lecroy HDO6104 12-bit 2.5 GHz oscilloscopes. The time delay between
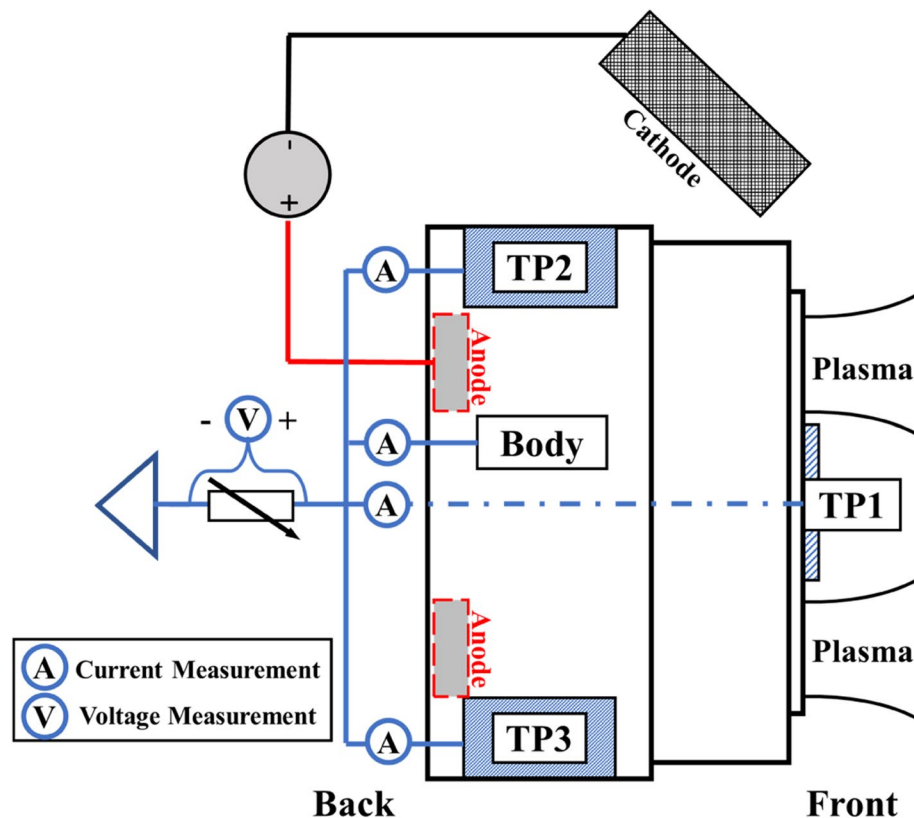

Fig. 3 Witness plate electrical configuration and measurement points

synchronous data capture of the two oscilloscopes is measured to be less than 26 ns. The time delay is relevant for results that assess the correlation between discharge current and witness plate current measurements. The oscilloscopes were configured to sample at 125 MS/s and collect 2 MS, giving a sample time of two femtoseconds. Results are derived from the arithmetic average of voltages and currents over the 2-fs measurement duration. The triggering for the data capture is handled by an Agilent 33250A Function / Arbitrary Waveform Generator. The triggering waveform is a 5-V amplitude square wave with a 0.5-s period. Table 1 lists the oscilloscope accessories used for current monitoring.

Correlation methods

In order to characterize the impact of artificial recombination pathways on thruster performance, metrics are needed to quantify correlation between thruster behavior and waveform response along the recombination pathway. The covariance is defined as the deviation of two jointly distributed random variables from their respective mean values:

$$\text{cov}(X, Y) = \sum_{i=1}^{N} \frac{\left((x_i - \overline{x})(y_i - \overline{y}) \right)}{N} \tag{2}$$

In Eq. (2), x and y represent discrete values of the random variables, $\overline{x}$ and $\overline{y}$ represent the mean values of the random variables over the sample interval, and N is the number of sample points. Covariance has units of $x_i y_i$; therefore, it is easier to assess correlation through the use of a normalized metric. The correlation coefficient is used with our data.

$$R(X, Y) = \frac{\text{cov}(X, Y)}{\sqrt{\text{cov}(X, X)\text{cov}(Y, Y)}} \tag{3}$$

where $cov(\_,\_)$ is the covariance of the terms in brackets, and $R(X, Y)$ is the correlation coefficient. A correlation coefficient of 1 indicates two waveforms are identically correlated, whereas a coefficient of -1 indicates anticorrelation. In this article, correlation coefficients greater than 0.7 are considered to indicate a strong correlation. For all the data analyzed and presented in this article, Eq. (3) was used to generate the correlation coefficient.

The cross-correlation function, $(f*g)$, is used to identify the time delay that maximizes the correlation between the two waveforms. The time delay corresponding to the largest absolute value of the cross-correlation function is interpreted as the time delay if and only if the two signals are strongly correlated. Cross-correlation is calculated by computing the convolution integral between two signals, as shown in Eqs. (4) and (5).

Table 1 Equipment used for current measurements

TP1 Current	Teledyne Lecroy CP30A High Sensitivity Active Current Clamp
TP2 Current	Teledyne Lecroy CP30A High Sensitivity Active Current Clamp
TP3 Current	Teledyne Lecroy CP30A High Sensitivity Active Current Clamp
HET Body Current	Teledyne Lecroy CP30 High Sensitivity Active Current Clamp
TP1–3, Body Voltage	Teledyne Lecroy PP18 10:1 Voltage Divider

$$(f * g)(\tau) \equiv \int_{-\infty}^{\infty} f(t)g(t + \tau)d\tau \tag{4}$$

$$(f * g)(\tau) \equiv \int_{-\infty}^{\infty} \left(f(t) - \bar{f}\right)\left(g(t + \tau) - \bar{g}\right)d\tau \tag{5}$$

In Eqs. (4) and (5), f is the reference waveform, g is the computed waveform, τ is the time offset, and t is time. The global mean $\bar{g}$ is subtracted from g in Eq. (5) to improve the sensitivity of this analysis. Peaks in the thruster discharge current are used as trigger events calculating the time delay since these are unique events in the sampling window. For all the data analyzed and presented in this article, Eq. (5) was used to calculate the time offset, τ, in cases in which the signals were correlated.

Results

Data presented in the results are subdivided into time-averaged and time-resolved measurements. Time-averaged measurements include average currents measured on the thruster body and witness plates. Time-resolved measurements include frequencies of the 1st and 2nd peaks of current oscillations and peak-to-peak current to ground on these surfaces. Statistical analysis of the correlation between discharge current oscillations and current oscillations measured on witness plates is provided at the end of the Results. All data in Time-Averaged and Time-Resolved sections are presented with body-to-cathode voltage as the independent variable.
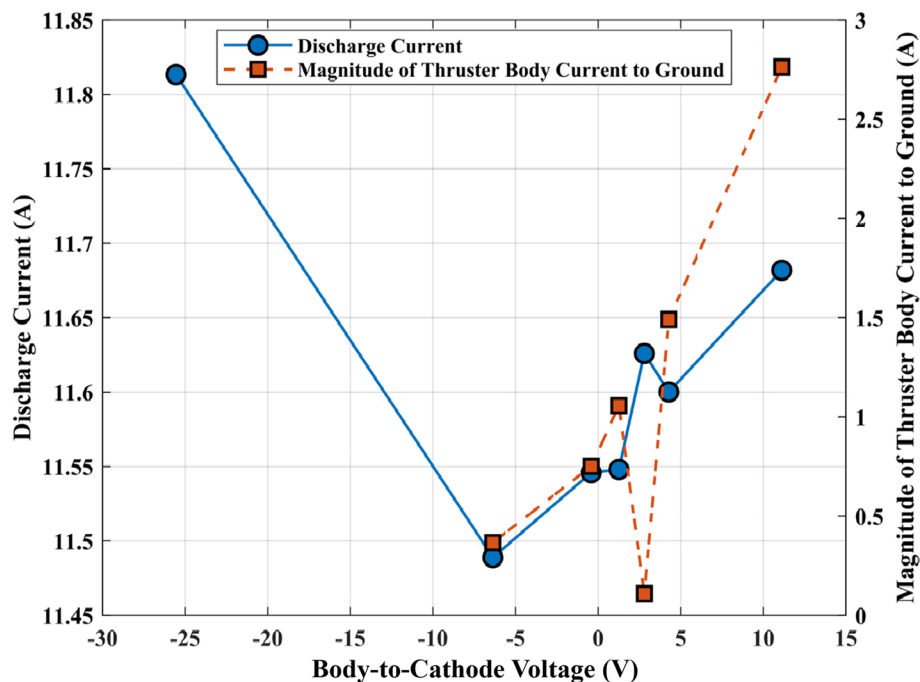

Fig. 4 Discharge current and thruster body current to ground as a function of body-to-cathode voltage

Time-averaged measurements

Discharge current

Figure 4 shows the average discharge current and the magnitude of thruster body current to ground. The convention for the current direction used in this study is that positively-charged particles generate positive current when flowing into the thruster body and eventually to ground. The thruster body serves as an electron collector at positive body-to-cathode voltage, and this results in negative current to ground using this circuit convention. However, it is easier to visualize the correlation between thruster body current to ground and discharge current if the magnitude is considered, which is the reason absolute values of electron current are plotted in Fig. 4. Witness plate contributions are also included in the current to ground measurement. At -25.5 V, the thruster body is electrically floating, and the discharge current is 11.81 A. As the body-to-cathode voltage increases, the discharge current decreases to a minimum at -6.37 V. At voltages greater than -6.37 V, the discharge current increases with body-to-cathode voltage. The 2.8 V measurement is a notable exception to the trend.

In Fig. 4, the thruster body current to ground demonstrates a similar correlation to the discharge current. At voltages greater than -6.37 V, the thruster body current to ground increases with body-to-cathode voltage, and the 2.8.

V measurement is the notable exception. This correlation is expected since positively-charged surfaces relative to cathode potential attract electrons, and the net electron current collected on the body should increase with voltage. At 2.8 V, the thruster discharge current increases abruptly, and the thruster body current to ground decreases abruptly. Unlike the other data points, the 2.8 V condition demonstrates anticorrelation between the discharge current and body current to ground. The cause of this anomalous measurement is suspected to be electrical resonance between the thruster body and the capacitors internal to the switch-mode power supply used for the thruster discharge.

Witness plates

Figure 5 shows current to ground as measured on the three witness plates. Note that the presented current is in units of mA. The total current collected by TP1, TP2, and TP3 at the 11.12 V condition represents less than 2% of the total current collected by the thruster body. Therefore, the witness plates affixed to the thruster serve as small charge flux regions compared to the remainder of the thruster body surface area. As with total thruster body current to ground, the magnitude of current to ground for individual witness plates increases with body-to-cathode voltage. TP2 and TP3 witness plates, located on the radial portion of the thruster, retain a negative current flux over the measurement range. This correlation indicates that these plates are electron collectors. TP2 also experiences a greater negative current flux than TP3 above the body-to-cathode voltage of 4.28 V. The positioning of TP2 could explain this correlation on the cathode-facing side of the thruster. TP1 experiences positive current flux until the 4.28 V condition, indicating that the plate serves as an ion collector at low body-to-cathode voltages.
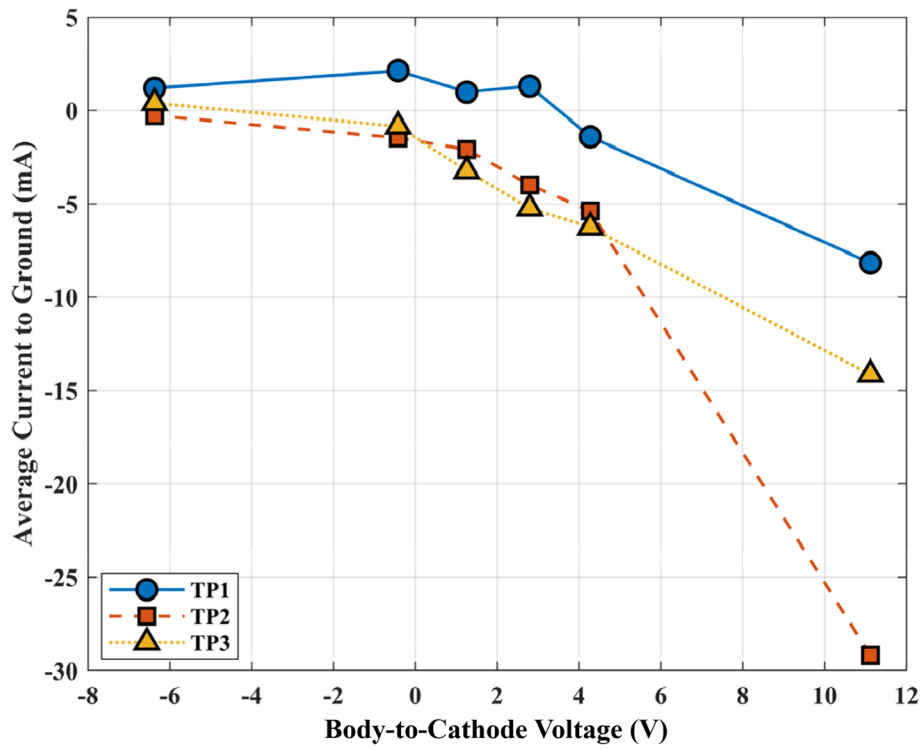
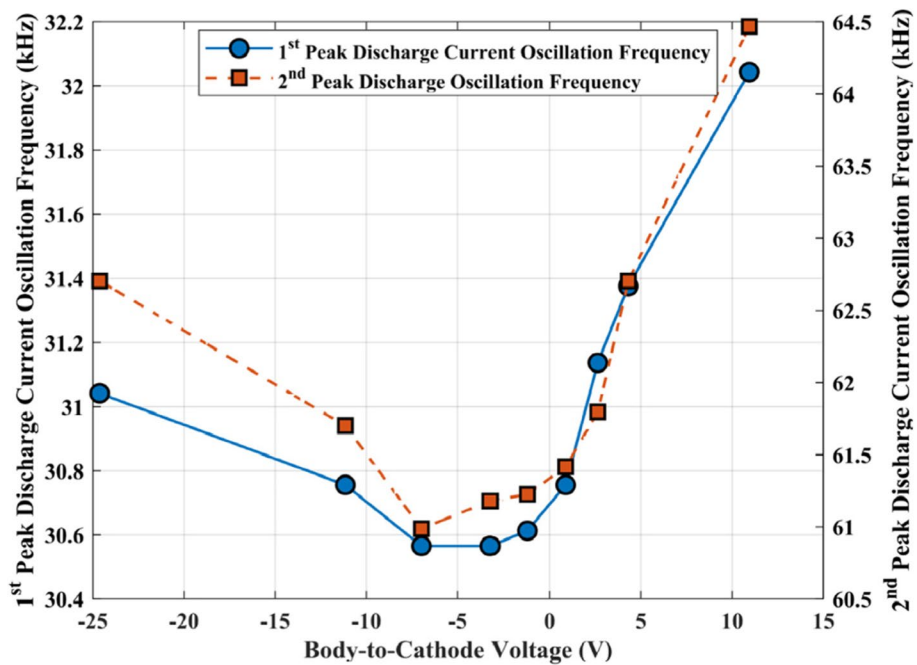**Fig. 5** Witness plates TP1, TP2, TP3 average current-to-ground as a function of body-to-cathode voltage

Fig. 6 Frequency of 1st and 2nd discharge current oscillation peaks as a function of body-to-cathode voltage

Time-resolved measurements

Discharge current and body current

Figure 6 shows the frequency of the 1st and 2nd spectral peaks in the discharge current. Separate y-axes are used for the data sets to allow the reader to compare the shapes of the correlations. The primary spectral peak varies between 30 and 33 kHz, within the frequency range where bulk plasma discharge oscillations are expected to occur [27]. The secondary spectral peak varies between 60 and 65 kHz. The frequency of both oscillation peaks displays a similar correlation with body-to-cathode voltage. A minimum oscillation frequency occurs for both peaks between -10 V and 0 V. As the body to cathode voltage moves away from the minima in either direction, oscillation frequency increases.

Figure 7 shows the peak-to-peak discharge current and thruster body current to ground. Peak-to-peak body current to ground appears to increase monotonically with peak-to-peak discharge current. Figure 8 shows a similar correlation in the discharge current and body current standard deviations.

Witness plates

Figures 9 and 10 show the peak-to-peak current to ground and standard deviation for the three witness plates, respectively. For all witness plates, the peak-to-peak current remains below 200 mA at body-to-cathode voltages below 4.27 V. Above 4.27 V, the peak-to-peak current to ground increases abruptly. The largest increase is observed on the TP1 witness plate, where peak-to-peak current increases from 100 mA to 750 mA. For the TP2 and TP3 witness plates, current increases from 150 mA to 650 mA and 200 mA to 450 mA, respectively.
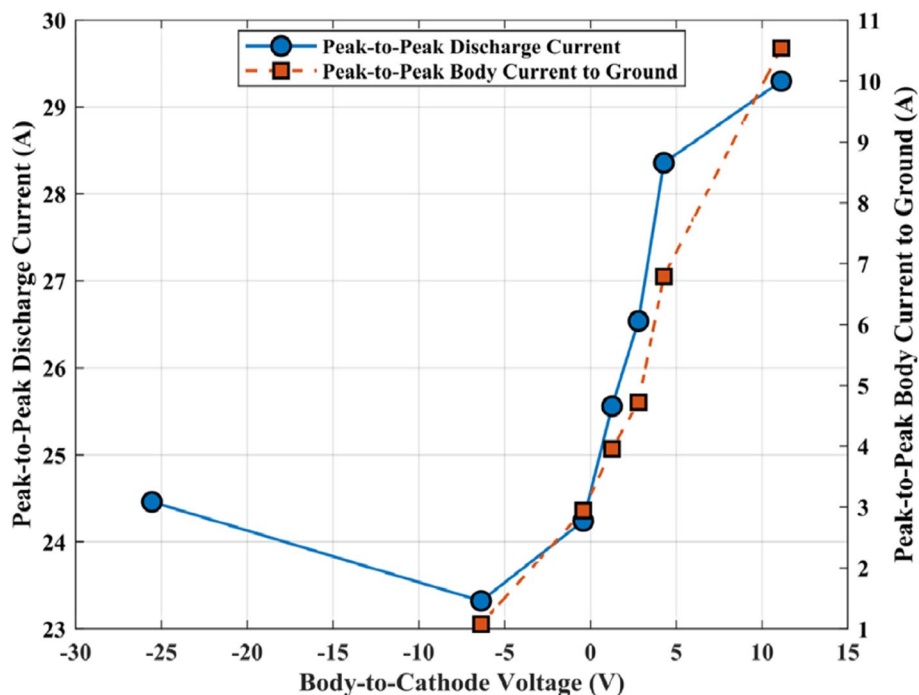

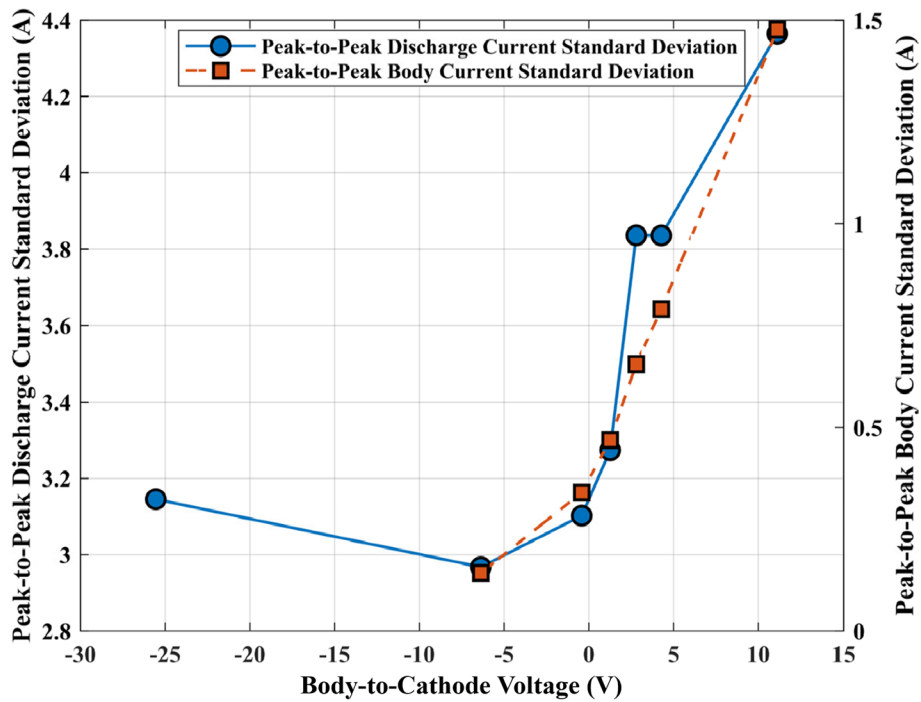**Fig. 7** Peak-to-peak discharge current and body current as a function of body-to-cathode voltage

Fig. 8 Peak-to-peak discharge current and body current standard deviation as a function of body-to cathode voltage
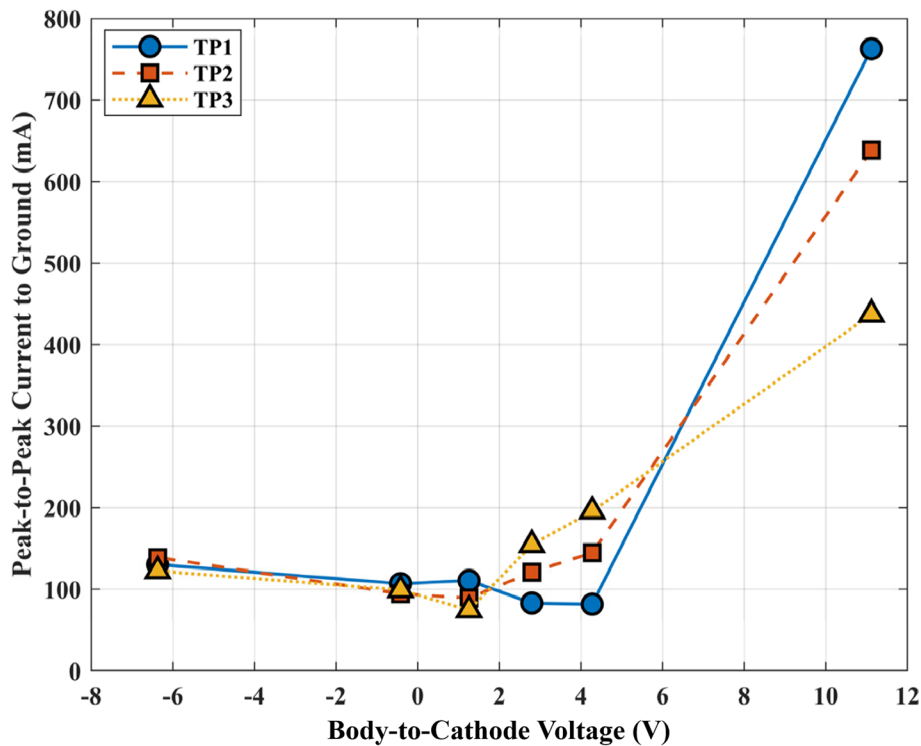

Fig. 9 Peak to peak current to ground as a function of body-to-cathode voltage
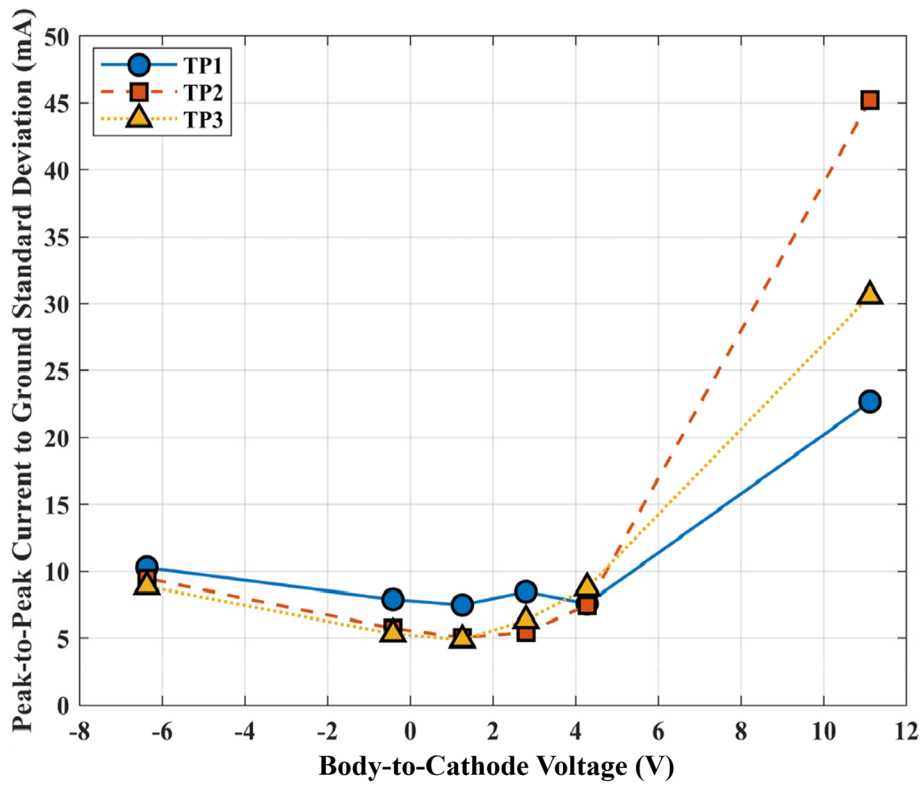
Fig. 10 Current to ground standard deviation as a function of body-to-cathode voltage
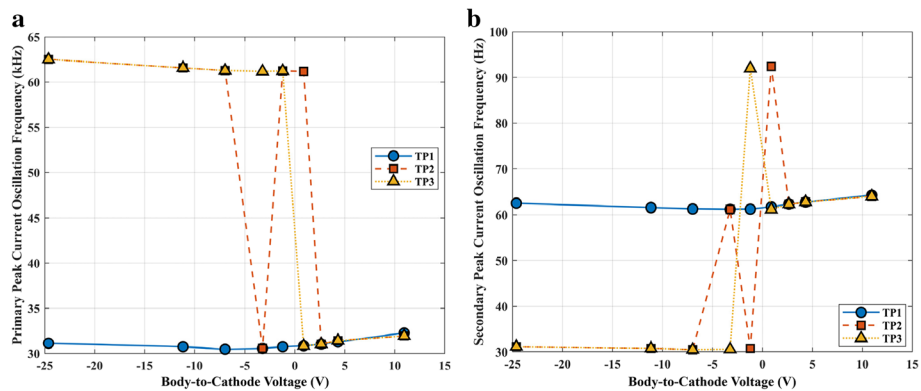

Fig. 11 **a** Primary current peak oscillation frequency as a function of thruster body-to-cathode voltage. **b**. Secondary current peak oscillation frequency as a function of body-to-cathode voltage

Figure 11a shows the frequency of the primary peak current oscillation on each witness plate. The correlation of TP1 oscillation frequency with body-to-cathode voltage exhibits similar behavior to the thruster body. A global minimum frequency of 30.4 kHz is observed at −6.98 V, and oscillation frequency increases monotonically with body-to-cathode voltage in the positive and negative directions. However, the increase in oscillation frequency is less than 2 kHz. In comparison to TP2 and TP3, TP1 peak current oscillation frequency is relatively insensitive to changes in body-to-cathode voltage.

TP2 and TP3 exhibit bimodal correlation with body-to-cathode voltage. Below -6.98 V, TP2, and TP3 current oscillation peaks are between 61 and 62 kHz. Between -6.98 V and 2.64 V, TP2 and TP3 enter a transition region where oscillation frequency shifts abruptly between 62 kHz and 31 kHz. In the transition region, the frequency can oscillate between bimodal limits. This behavior is observed for TP2, where the current oscillation frequency increases from 30 kHz to 61 kHz between -3 V and 3 V. The current oscillation peaks for TP1, TP2, and TP3 are near 32 kHz at body-to-cathode voltages above 2.64 V.

Figure 11b shows the frequency of the secondary peak current oscillation on each witness plate. The frequency of the TP1 secondary peak is centered at approximately 62 kHz and is insensitive to changes in body-to-cathode voltage. TP2 and TP3 exhibit bimodal behavior for the secondary current oscillation peak. Both TP2 and TP3 current oscillations are at 30 kHz below -6.9 V. A transition region occurs between -6.9 V and 2.64 V, and above 2.64 V, TP2 and TP3 oscillate at 62 kHz. In the transition region, TP2 and TP3 secondary peak current oscillation frequencies are also observed to increase over a single voltage step from 30 kHz to 92 kHz before decreasing to 62 kHz.

Correlation of discharge current and witness plate measurements

Figure 12a, b, and c show the time delay and correlation coefficients as a function of cathode-to-body voltage for the three witness plates. For TP1, the time delay increases monotonically with body-to-cathode voltage above -6.4 V. The time delay varies from 6.67 μs at 11.1 V to 3.29 μs at -6.4 V. Between 0 V and 11.1 V, time delay decreases by
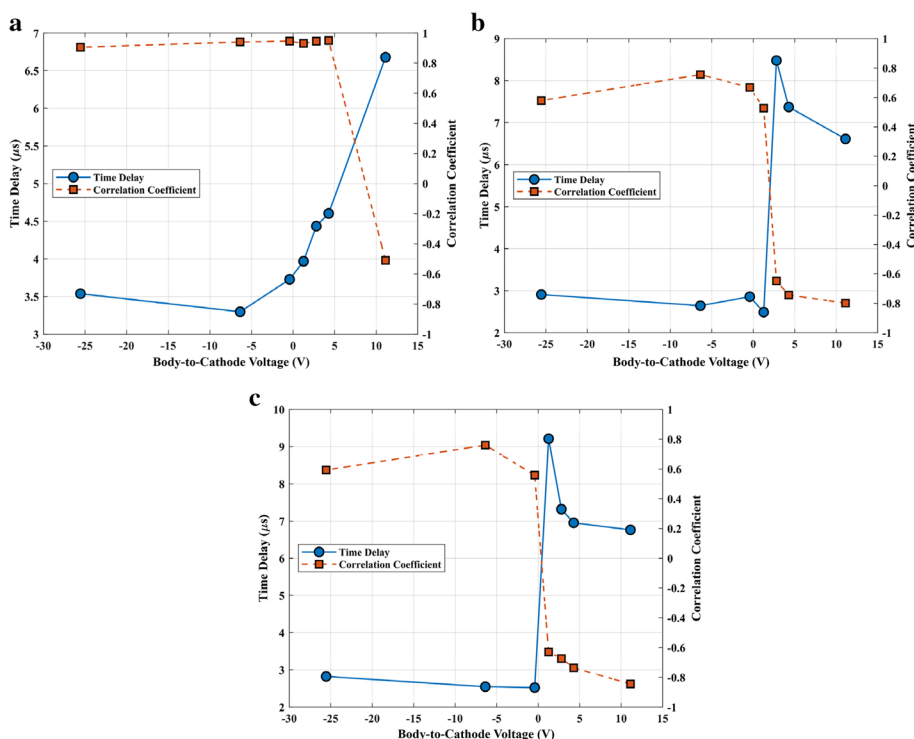

Fig. 12 **a** TP1 witness plate current to ground time delay and correlation coefficient. **b** TP2 witness plate current to ground time delay and correlation coefficient. **c** TP3 witness plate current to ground time delay and correlation coefficient

87% of the total range, indicating time delay is strongly correlated with body potential when the thruster body voltage is positive relative to the cathode. The correlation between TP1 current to ground and the discharge current remains strong (~ 0.9) up to the 11.1 V condition, where the waveforms become weakly anti-correlated.

The TP2 and TP3 time delays and correlation coefficients exhibit bimodal behavior. Starting at the -25.5 V body-to-cathode measurement, time delays are in the range of 2.5–3.0 μs and are insensitive to changes in body-to-cathode voltage. Between -3.0 V and 3.0 V, time delays increase abruptly to 8.5–9.5 μs. As the time delay increases, the correlation coefficients invert from strong correlation to strong anticorrelation. As body-to-cathode voltage increases further, time delays decrease from peak values to the range of 6.5–7.5 μs.

Discussion

The plasma environment surrounding the thruster body

The plasma environment surrounding the thruster body is divided into two regions: (1) Thruster face (TP1) and (2) Thruster circumference (TP2 and TP3). Figure 13 shows that the electric field of the anode, thruster magnetic field, and cathode position maintain electron number densities at the thruster face on the order of 10^{15}–10^{18} m^{-3} [8, 28–30]. The electron Hall parameter in this region is significantly larger than unity [8], and electron motion is parallel to magnetic field lines. In annular HET geometries, magnetic field lines converge at the center pole face where the inner solenoid is located. The magnetic field directs electrons towards the discharge channel and confines electrons at the thruster face. Magnetic field lines reconnect to the thruster body on the thruster
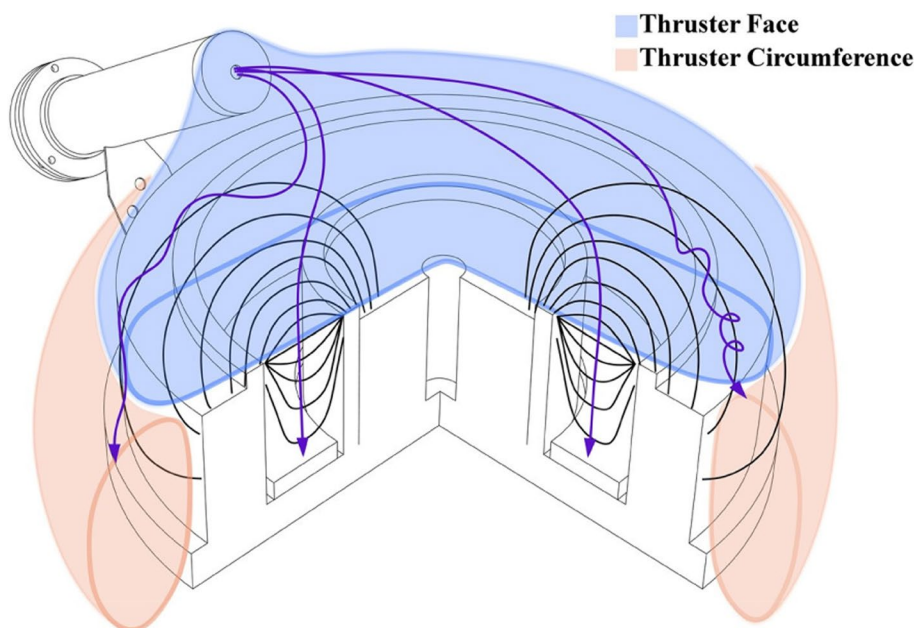
Fig. 13 Plasma regions surrounding the thruster body. Cathode position and the magnetic field confine electrons at the thruster face and yield number densities on the order of 10^{15}–10^{18} m^{-3}. Some electrons thermalized along magnetic field lines propagate to the thruster circumference, where electron number densities are lower. Note that the magnetic field lines represent a thruster design lacking a separatrix and are for illustrative purposes only

circumference where the TP2 and TP3 witness plates are located. Electrons in this region are also magnetized [8]; however, the cathode position and reduced magnetic flux density produce a lower electron number density in these circumferential regions than on the exit face. A separatrix may isolate the pole face from the circumferential region in thruster designs that utilize discrete outer coils [31, 32]. Since electrons are magnetized, the separatrix isolates the electron populations at the exit face from the circumferential region in these thruster designs.

If the surface of the thruster body is at the local plasma potential, then no electric field exists to accelerate or inhibit the flux of charged particles to the surface. However, the plasma potential around the thruster body exhibits spatial nonuniformity [28]. Therefore, sheaths are expected to exist regionally between the thruster body and the surrounding plasma environment in almost all circumstances. Sheaths form to isolate plasma from surfaces with electrical properties that favor the collection of charge species in a manner that violates quasineutrality. Plasma sheaths are nonquasineutral, and particle dynamics in sheaths differ significantly from behavior in the bulk plasma.

Floating thruster body

When the thruster body is electrically isolated from the thruster's electrical circuit, the thruster's surfaces are let to float relative to the plasma. In this case, the plasma will form electron repelling sheaths to maintain zero net charge flux into the thruster body. The potential difference across the sheath (ϕ_f) is dependent on the local electron temperature and is equal to $\varphi_f = \frac{kT_e}{e} \ln \left(\sqrt{\frac{2m_i}{\pi m_e}} \right)$, where $\frac{kT_e}{e}$ is the electron temperature in eV and $\frac{m_i}{m_e}$ is the ion-to-electron mass ratio. In the case of xenon propellant, the floating potential is $\sim 6\frac{kT_e}{e}$. The electron temperature in the vicinity of the thruster varies spatially. However, the highest values of electron temperature in the vicinity of the thruster body are expected to take place close to the front poles, closest to the discharge channel exit plane. The electron temperature near the front plates was measured and numerically calculated for various HETs [33–37] and was found to be in the range 2–5 eV, whereas the most common electron temperature was approximately 4 eV. Since there are no experimental or numerical data on the electron temperature next to the surfaces of the T-140 HET presented in this study we use the data published on a similar HET operating at the same discharge power level of 3 kW – the NASA-300 M HET. Past studies show that the electron temperature near the poles of the NASA-300 M thruster is in the 4–5 eV range [36]. The expected floating voltage of such a thruster is 24–30 V below ground potential, and in line with the measured floating voltage of -25 V of the T-140 in this study. Similar values of floating thruster body potential at a discharge voltage of 300 V were also measured for a 2-kW magnetically shielded HET (-22 V) [15] and the H6 HET (-33.2 V) [13].

It is interesting to note that since the electron temperature in the acceleration region increases with an increase in the discharge voltage [36, 38, 39], we expect to see more negatively biased thruster body floating potentials under these high discharge voltage operating conditions. This was experimentally validated by Watanabe [15], who measured floating body potential values of down to -75 V at a discharge voltage of 800 V,

and Peterson [12], who measured floating body potential values of down to $-45\,\text{V}$ at a discharge voltage of $600\,\text{V}$.

Lastly, insulating the front plates of the Hall thruster may bring the thruster body floating potential closer to ground as no charged particles are allowed to flux into the thruster front plates, and most interaction with plasma occurs in the thruster circumference, where the electron temperature is lowest. This was also experimentally demonstrated by Peterson [12].

Biased thruster body

When the thruster body is biased to potentials above the floating potential, then non-equal electron and ion fluxes will be exerted on the thruster surface, and either an electron-repelling or electron-attracting sheaths will be formed, although in most cases electron repelling sheaths are most prominent, and the plasma-to-surface potentials need to be positive to form an electron attracting sheath situation. The resulting net current is the current leaking through the thruster body. Assuming Maxwellian electrons near the thruster surface, the electron current into the thruster (I_e) is $A_s e \cdot \frac{1}{4}\sqrt{\frac{8kT_e}{\pi m_e}} \cdot 0.606 \cdot n_0 \cdot \exp\left(-\frac{e\Delta\varphi}{kT_e}\right)$ where A_s is the surface area exposed to the plasma, $\sqrt{\frac{8kT_e}{\pi m_e}}$ is the electron mean thermal velocity, n_0 is the local plasma density and $\Delta\phi$ is the potential difference between the local plasma potential and the thruster body potential, also denoted by the sheath voltage drop. The ion current into the thruster body (I_i) is roughly constant with the sheath voltage drop and is $A_s 0.606 n_0 e \sqrt{\frac{kT_e}{m_i}}$ where $\sqrt{\frac{kT_e}{m_i}}$ is the Bohm velocity that ions enter the sheath. The net current density into the thruster body is dependent on the local electron temperature, local plasma density, thruster body surface area exposed to plasma, and the difference between the local plasma potential in the vicinity of the exposed surface and thruster body potential. When biasing the thruster body closer to ground (more positive), the sheath voltage drop becomes less negative to allow more electrons to reach the thruster surface. As the thruster body potential increases, the sheath voltage drop decreases, although still electron-repelling, and a larger electron current is collected by the thruster surfaces exposed to the plasma. If the sheath potential is reversed and becomes electron-attracting, then the expected electron current into the thruster body surface may take values of more than an order of magnitude higher than the currents associated with electron-repelling sheaths [40].

It is also important to note that the plasma environment surrounding different sections of the thruster body, and specifically the plasma density, is non-homogeneous. This may cause a situation in which different sections of the thruster may locally conduct different currents according to the local plasma properties. In the analysis presented hereafter, we will assume uniform plasma density along specific sections of the thruster body.

Since the literature contains information mainly on plasma parameters in the near plume region, we can estimate the net current into the front plates of the thruster body as the thruster body potential is varied closer to ground potential. The surface area of TP1 is $6.8 \times 10^{-3}\,\text{m}^2$. We estimate a local plasma density of $10^{15}\,\text{m}^{-3}$ [41, 42] and a potential difference of $10\,\text{V}$ between the plasma potential and the thruster body
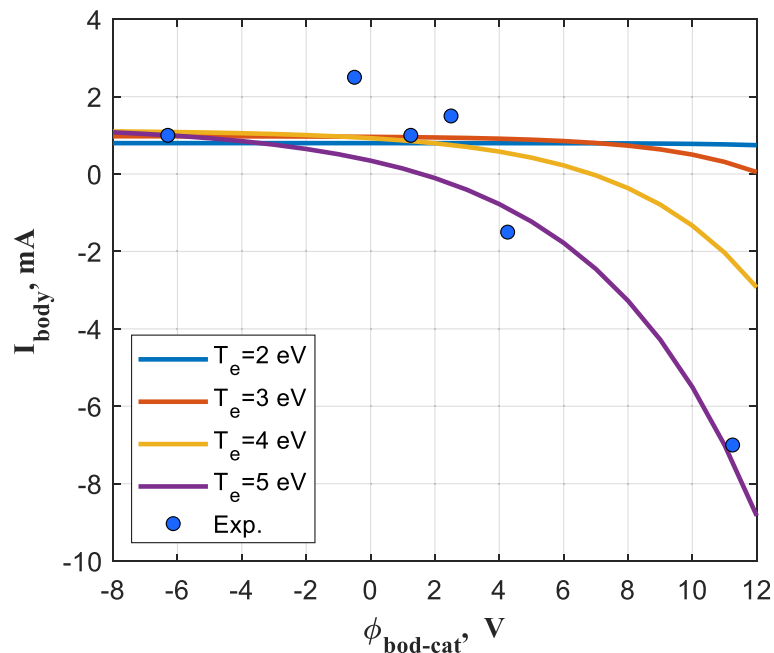
Fig. 14 Estimated net current through the thruster body as a function of body-to-cathode potential for electron temperatures in the range 2–5 eV. Plasma density is assumed $10^{-15}\,\mathrm{m}^{-3}$, and plasma to cathode potential is assumed 10V

potential [14, 36]. We examine electron temperature values in the range of 2–5 eV as reported in the literature.

Figure 14 presents the net current into the thruster body as a function of the thruster body potential relative to the cathode potential. We maintain the convention of the direction of current as positive when positively-charged particles flux into the thruster body. It can be observed in the figure that the net current through the front witness plate (TP1) exhibits the same behavior and has the same order of magnitude as the measured current through TP1. It can also be seen that an electron temperature of 4–5 eV aligns best with the experimental data, as was found for the case of a floating thruster body potential.

The electron temperature close to the thruster circumference is lower, thus producing a low sheath voltage drop and allowing large electron currents to be collected by the thruster body, as was observed in Fig. 5 for TP2 and TP3. Since the electron density is higher closer to the cathode, where TP2 is positioned, we expect higher electron currents to be collected in these regions of the thruster body, as was also demonstrated in Fig. 5.

When large sections of the thruster body are exposed to the plasma, much higher net current is expected to flow through the thruster body, as reported in the literature. These currents, which are electron dominated, may take as high as 13.6% of the discharge current [12], thus reducing system efficiency.

In HETs where the discharge is pushed downstream, we expect to see a larger difference between the plasma potential and thruster body potential. These larger potential differences are expected to drive down the electron flux into the thruster surfaces and overall reduce the net current conducted through the thruster body.

Significance of polarity and magnitude of the body-to-cathode voltage

Electrons in the vicinity of the thruster body are sourced from the cathode. Therefore, the cathode sets the initial temperature of electrons in the plasma environment surrounding the thruster body. In the region surrounding the thruster circumference, the magnetic field of the thruster is relatively weak but still strong enough to confine electron motion to magnetic field lines. Therefore, electron temperature in this region should be near the cathode emission temperature, and the potential difference between the thruster body and cathode likely represents the potential gradient in the local plasma sheath. As the thruster body voltage approaches the cathode voltage, the electron repelling sheaths around the thruster circumference are reduced and allow for a larger electron current to flux into the thruster body in these regions.

At the thruster exit face, heating occurs as electrons gain kinetic energy diffusing towards the anode across magnetic field lines. The plasma temperature in this region is hotter relative to the cathode, and charge exchange collisions result in the creation of an ion population that recombines at the thruster face. These features change the current collection and recombination behavior of the thruster body at the exit face. Therefore, the discussion of results is subdivided to consider the thruster body circumference and the exit face independently.

Thruster body circumference

Figure 5 shows that the TP2 and TP3 witness plates begin to collect appreciable electron current when the body-to-plasma voltage becomes positive. At negative body-to-cathode voltage, some electrons in the local plasma environment possess adequate kinetic energy to overcome the adverse sheath potential and recombine at the thruster body circumference. This population of electrons produces a low negative current of $-0.42\,\text{mA}$ at the $-0.42\,\text{V}$ condition.

As body voltage increases above cathode voltage, current collection on the TP2 and TP3 witness plates increases monotonically. Although the reduced densities (assumed $< 10^{-15}\,\text{m}^{-3}$) and electron temperatures (approximately $1-2\,\text{eV}$) in these regions, the Debye length, thus the sheath size, is approximately $1\,\text{mm}$, which is lower than the characteristic length of the thruster. We thus conclude that sheath expansion in this region is not considerable, and the sheath collects charge fluxes according to the potential difference established between the local plasma and thruster body.

Figures 9 and 10 show that peak-to-peak current and standard deviation increase monotonically above $1.25\,\text{V}$ for the TP2 and TP3 witness plates. Therefore, the quantity of electrons collected on the circumference of the thruster body varies with time, and the amplitude of current oscillations increases with body-to-cathode voltage. Figure 11a and b show that the frequency of the current oscillations on the circumferential witness plates also varies with body-to-cathode voltage. Below $-6.98\,\text{V}$, the peak oscillation frequency on the TP2 and TP3 witness plates couples to the secondary peak in the discharge current oscillation. Above $2.64\,\text{V}$, the peak oscillation frequency couples to the primary discharge current oscillation peak.

Figure 12b and c quantify the relationship between peak-to-peak current oscillations measured on the witness plates and oscillations in the discharge current. At negative body-to-cathode voltages, the discharge current and witness plate waveforms are correlated, and

oscillations occur synchronously. At positive body-to-cathode voltages, the current waveforms oscillate asynchronously. Peaks in the discharge current may deplete electrons thermalized along magnetic field lines in the vicinity of the thruster exit face. If thruster body voltage is positive relative to the cathode, the depletion may reduce the number of electrons in the local plasma environment available to recombine at the thruster body circumference. Therefore, discharge current peaks could produce minima in current collected along the circumference of the thruster body. At negative body-to-cathode voltages, the coupling may not exist because the plasma sheath that forms around the thruster body prevents electrons associated with the thruster discharge oscillations from interacting with the thruster body. The thruster circumference would instead couple to the secondary peak in the discharge current oscillation. Net currents collected on recombination surfaces do not provide adequate evidence to substantiate or refute this hypothesis. Direct measurements are needed of the electron dynamics in the region around the thruster body to fully understand the results presented in Fig. 12b and c.

Thruster face

Figure 5 shows that the TP1 witness plate collects current until the body-to-cathode voltage reaches 4.28 V. The magnitude of the collected ion current remains between 1 and 3 mA irrespective of body-to-cathode voltage. The insensitivity to body-to-cathode voltage suggests that the ions are collected through a strongly electron-repelling sheath, while the positive flux depends mainly on the Bohm velocity. As body-to-cathode voltage becomes less negative, the electron repelling sheath allows for a higher stream of electrons to flux into the front face.

Figure 9 shows that the magnitude of peak-to-peak current on the TP1 witness plate does not increase until the body-to-cathode voltage is greater than 4.28 V. The cause of the positive offset from the body-to-cathode crossover voltage is unknown, but it is likely related to the strong magnetic field at the thruster face. Magnetic field lines associated with the discharge channel reconnect to the thruster body at the exit face, and there are relatively large gradients in the strength of the magnetic field. Therefore, electron temperature in this region likely exhibits spatial nonuniformity since electrons thermalized along magnetic field lines closer to the channel will possess greater kinetic energy than electrons further from the channel. The temperature gradients make it difficult to draw conclusions about electron motion in the sheath at the thruster face without knowing more about the electron energy distribution. Unlike electrons, the motion of charge exchange ions produced in this region is not significantly affected by the magnetic field.

Figure 11a and b show that the thruster face remains coupled to the primary and secondary oscillation peaks in the discharge current irrespective of body-to-cathode voltage. Compared to the circumferential region of the thruster body, the thruster face is exposed to the ionization and acceleration regions where discharge current oscillations originate. Therefore, these electron populations couple to the exit face irrespective of the body-to-cathode voltage. Figure 12b shows the time delay and correlation coefficient for the TP1 witness plate. The transition from correlation to anticorrelation occurs at 4.28 V instead of 0 V for the circumferential region. Unlike the circumferential region, a monotonic increase in time delay is observed between -5 V and 5 V.

Discharge current oscillations and power dissipation in the thruster body

Figure 6 shows that the frequency of the first and second peaks of the discharge current oscillations are minimized as cathode voltage approaches the body potential. Peaks in the discharge current are associated with depleting the neutral populations in the discharge channel through bulk ionization events [43–45]. However, predator-prey models of the breathing mode do not examine the relationship between bulk ionization events and electron availability in the channel and exit face regions. Figure 11a and b show that minimization of the current oscillation frequency occurs on the TP1 witness plate as body voltage approaches the cathode voltage. Therefore, electrons couple discharge current oscillations originating in the channel to surfaces on the thruster body. We postulate that as the body potential approaches cathode voltage, the sheath voltage fall becomes less negative; more electrons are collected by the thruster body, allowing fewer electrons to enter the discharge channel. In other words, the thruster body serves as an electron sink, pulling in electrons that otherwise would have entered the discharge chamber. This situation results in a shortage of electrons reaching the ionization region, therefore, extending the ionization front downstream towards the thruster's exit plane. Fife showed that the length of the ionization region is inversely proportional to the oscillation frequency ($L_i \propto \frac{1}{f}$) [46]. Consequently, the widening of the ionization front extends the time period of ionization oscillations and reduces the oscillation frequency. Similar breathing mode frequency behavior was observed when comparing internal and external cathode by Hofer [16]. In his study, Hofer suggested that since the supply of electrons is farther downstream when employing an external cathode, then the ionization region extends downstream. This, in turn, led to a reduction in oscillation frequency. Nevertheless, the postulation presented here should be corroborated with measurements demonstrating an ionization length shift with variations with thruster body potential.

Conclusion

This work demonstrates that body-to-cathode voltage controls the accessibility of the thruster body recombination pathway. A positive body-to-cathode voltage allows electrons to recombine on the thruster circumference in designs that lack a magnetic separatrix. As the body voltage becomes positive relative to the cathode, the magnitude of the collected current on the thruster body increases because the effective electron capture area of the sheath surrounding the thruster body circumference increases. Negative body-to-cathode voltages likely prevent an electron population associated with the primary discharge current oscillation peak from recombining at the thruster circumference due to the existence of an electron-repelling sheath. The peak oscillation frequency on the thruster circumference instead couples to the secondary peak in the discharge current.

Setting the body potential equal to the cathode potential minimizes primary and secondary peaks in the oscillation frequency of the thruster discharge current. Since discharge current oscillations couple to surfaces on the thruster body, minimizing the frequency of the discharge current also minimizes the frequency of current oscillations measured on the thruster body surfaces. The physical mechanism that causes discharge current oscillations to be minimized when thruster body potential matches the cathode

potential is not entirely understood. Since electrons are the more mobile charge species in the local plasma environment, it is possible that the thruster body could serve as an energy source or sink that alters the frequency of discharge current oscillations depending on the body-to-cathode voltage.

The Child-Langmuir sheath model provides a first-order approximation of ion current collection characteristics on the thruster exit face when an electron repelling sheath is present, and the sheath is thin compared to the surface area of the collector. However, the accuracy of the model is limited due to strong magnetic field gradients and non-Maxwellian electron energy distributions near the thruster body. More refined models of sheath characteristics are needed to describe the sheath around the thruster body circumference. Specifically, additional measurements of the electron number densities in this region are needed to characterize the sheath thickness.

Nomenclature

A_s	surface area, meters^2
ε_0	permittivity of free space, Farads per meter
f	reference waveform
g	computed waveform
$\bar{g}$	global mean
I	current test point, Amperes
J_i	ion current, Amperes
k_b	Boltzmann constant, Joules per Kelvin
m_i	Ion mass, Kilograms
n_j	species number density, meter^{-3}
n_∞	ion number density far from the sheath, meter^{-3}
P_b	vacuum chamber base pressure, Torr
P_c	corrected vacuum chamber base pressure, Torr
P_i	indicated vacuum chamber background pressure, Torr
q_e	electron charge, Coulombs
q_j	species charge, Coulombs
R_d	Debye radius, meters
T_e	electron temperature, Kelvin
T_j	species temperature, Kelvin
V	voltage test point, Volts
V_B	Bohm voltage, Volts
V_D	discharge voltage, Volts
x_i, y_i	discrete random variables
$\bar{x}, y$	average value of the discrete random variables
t	time, seconds
τ	time offset, seconds

Walker *et al. Journal of Electric Propulsion*   (2022) 1:18

Page 23 of 24

analysis were performed by J. Walker, and D. Lev. V, Khayms, and D. King assisted with the items to consider during the experimental setup to catch pertinent physical process and interpretation of the data. The first draft of the manuscript was written by J. Walker, and all authors commented on previous versions of the manuscript. The author(s) read and approved the final manuscript.

Availability of data and materials
I declare that the authors have no competing interests as defined by Springer, or other interests that might be perceived to influence the results and/or discussion reported in this paper.
The authors hold all rights for all of the material presented in the manuscript.

Declarations

Ethics approval and consent to participate
The corresponding author has read the Springer journal policies on author responsibilities (opens in a new window) and submits this manuscript in accordance with those policies.

Consent for publication
All authors have approved the manuscript and agree with its submission to the Journal of Electric Propulsion.

Competing interests
I declare that the authors have no competing interests as defined by Springer, or other interests that might be perceived to influence the results and/or discussion reported in this paper.

References

1. Walker MLR (2005) Effects of facility backpressure on the performance and plume of a hall thruster. University of Michigan
2. Huang W, Kamhawi H, Haag T (2016) Facility effect characterization test of NASA's Hermes Hall Thruster. 52nd AIAA/SAE/ASEE Joint Propulsion Conference. Salt Lake city, UT. https://doi.org/10.2514/6.2016-4828
3. Dankanich JW, Walker M, Swiatek MW, Yim JT (2017) Recommended practice for pressure measurement and calculation of effective pumping speed in electric propulsion testing. J Propuls Power 33(3):668–680. https://doi.org/10.2514/1.B35478
4. Snyder JS, Lenguito G, Frieman JD, Haag TW, Mackey JA (2020) Effects of background pressure on SPT-140 hall thruster performance. J Propuls Power 36(5):668–676. https://doi.org/10.2514/1.B37702
5. Walker JA, Frieman JD, Walker ML, Khayms V, King D, Peterson PY (2016) Electrical facility effects on hall-effect-thruster cathode coupling: Discharge oscillations and facility coupling. J Propuls Power. 32(4):844–55. https://doi.org/10.2514/1.b35835
6. Walker JA, Frieman JD, Walker MLR, Khayms V, King D, Peterson PY (2016) Electrical facility effects on hall-effect-thruster cathode coupling: discharge oscillations and facility coupling. J Propuls Power 32(4):844–855. https://doi.org/10.2514/1.B35835
7. Walker JA, Langendorf SJ, Walker MLR, Khayms V, King D, Peterson P (2016) Electrical facility effects on hall current thrusters: Electron termination pathway manipulation. J Propuls Power 32(6):1365–1377. https://doi.org/10.2514/1.B35904
8. Frieman JD, Walker JA, Walker MLR, Khayms V, King DQ (2016) Electrical facility effects on hall thruster cathode coupling: performance and plume properties. J Propuls Power 32(1):251–264. https://doi.org/10.2514/1.B35683
9. Frieman JD, King ST, Walker MLR, Khayms V, King D (2014) Role of a conducting vacuum chamber in the hall effect thruster electrical circuit. J Propuls Power 30(6):1471–1479. https://doi.org/10.2514/1.B35308
10. Frieman JD, Brown NP, Liu CY, Liu TM, Walker MLR, Khayms V, King DQ (2018) Electrical facility effects on faraday probe measurements. J Propuls Power 34(1):267–269. https://doi.org/10.2514/1.B36467
11. Frieman JD, Brown NP, Liu CY, Liu TM, Walker MLR, Khayms V, King DQ (2018) Impact of propellant species on hall effect thruster electrical facility effects. J Propuls Power 34(3):600–613. https://doi.org/10.2514/1.B36566
12. Peterson PY et al (2016) NASA's Hermes hall thruster electrical configuration characterization. In: 52nd AIAA/SAE/ASEE Joint Propulsion Conference. https://doi.org/10.2514/6.2016-5027
13. McDonald MS (2012) Electron transport in hall thrusters. Doctorate of Philosophy, Department of Aerospace Engineering, The University of Michigan, Ann Arbor
14. Katz I, Lopez Ortega A, Goebel DM, Sekerak MJ, Hofer RR, Jorns BA, Brophy JR (2016) Effect of solar array plume interactions on hall thruster cathode common potentials. In: In the 14th spacecraft charging technology conference. ESA/ESTEC, Noordwijk
15. Watanabe H et al (2020) Performance evaluation of a two-kilowatt magnetically shielded hall thruster. J Propuls Power 36(1):14–24. https://doi.org/10.2514/1.b37550
16. Hofer RR, Anderson JR (2014) Finite pressure effects in magnetically shielded hall thrusters. In: 50th AIAA/ASME/SAE/ASEE joint propulsion conference. https://doi.org/10.2514/6.2014-3709

Walker *et al. Journal of Electric Propulsion*   (2022) 1:18

Page 24 of 24

17. Koppel C, Marchandise F, Estublier D, Jolivet L (2004) The Smart-1 electric propulsion subsystem in flight experience. In: Presented at the 40th AIAA/ASME/SAE/ASEE joint propulsion conference and exhibit, Fort Lauderdale, Florida

18. Passaro A, Vicini A, Nania F, Biagioni L (2010) Numerical rebuilding of SMART-1 hall effect thruster plasma plume. J Propuls Power 26(1):149–158. https://doi.org/10.2514/1.36821

19. Kieckhafer A, Walker MLR (2011) Recirculating liquid nitrogen system for operation of cryogenic pumps. In: Presented at the 32nd international electric propulsion conference, Wiesbaden, Germany

20. McLean C, McVey J, Schappell T (1999) Testing of a U.S.-built HET system for orbit transfer applications. In: Presented at the 35th joint propulsion conference and exhibit, Los Angeles, CA, U.S.a

21. Santos R, Ahedo E, Raitses Y, Fisch NJ (2011) Transitional regime in the start-up process of conventional hall thrusters, In the 32nd International Electric Propulsion Conference. Wiesbaden, Germany. IEPC-2011-59.

22. Crofton MW, Pollard J (2013) Thrust augmentation by charge exchange. In: Presented at the 49th AIAA/ASME/SAE/ASEE joint propulsion conference, San Jose, CA

23. Boyd ID, Crofton MW (2014) Numerical momentum tracking for a hall thruster plume. In: Presented at the 50th AIAA/ASME/SAE/ASEE joint propulsion conference, Cleveland, OH

24. Sekerak MJ, Hofer RR, Polk JE, Jorns BA, Mikellides IG (2015) Wear testing of a magnetically shielded hall thruster at 2000 s specific impulse. In: Presented at the 30th international symposium on space technology and science, 34th international electric propulsion conference and 6th Nano-satellite symposium, Hyogo-Kobe, Japan

25. Mikellides IG, Lopez Ortega A, Jorns B (2014) Assessment of pole Erosion in a magnetically shielded hall thruster. In: Presented at the 50th AIAA/ASME/SAE/ASEE joint propulsion conference, Cleveland, OH

26. Goebel D and Katz I (2008) Fundamentals of Electric Propulsion: Ion and Hall Thrusters. Wiley, Hoboken

27. Choueiri EY (2001) Plasma oscillations in hall thrusters. Phys Plasmas 8(4):1411. https://doi.org/10.1063/1.1354644

28. Sommerville JD, King LB (2011) Hall-effect thruster--cathode coupling, part II: ion beam and near-field plume. J Propuls Power 27(4):754–767. https://doi.org/10.2514/1.50124

29. Washeleski RL, Meyer EJ, King LB (2013) Application of maximum likelihood methods to laser Thomson scattering measurements of low density plasmas. Rev Sci Instrum 84(10):105101. https://doi.org/10.1063/1.4821980

30. Vincent B, Tsikata S, Mazouffre S (2020) Incoherent Thomson scattering measurements of Electron properties in a conventional and magnetically-shielded hall thruster. Plasma Sources Sci Technol 29(3):035015. https://doi.org/10.1088/1361-6595/ab6c42

31. Conversano, R. W. Low-power magnetically shielded hall thrusters. Dissertation. University of California Los Angeles, 2015

32. Sommerville JD, King LB (2011) Hall-effect thruster--cathode coupling, part I: efficiency improvements from an extended outer pole. J Propuls Power 27(4):744–753. https://doi.org/10.2514/1.50123

33. Haas J, Gallimore AD (2000) An investigation of internal ion number density and Electron temperature profiles in a laboratory-model hall thruster. In: 36th AIAA/ASME/SAE/ASEE joint propulsion conference and exhibit. https://doi.org/10.2514/6.2000-3422

34. Gray T, Williams G, Kamhawi H, Frieman J, Mikellides I (2019) Non-intrusive characterization of the Wear of the HERMeS thruster using optical emission spectroscopy. In: The 36th international electric propulsion conference, Vienna, Austria IEPC-2019-841

35. Perot C et al (1999) 35th AIAA/ASME/SAE/ASEE joint propulsion conference and exhibit, 20-24 June 1999, Los Angeles, California. In: Characterization of a laboratory hall thruster with electrical probes and comparisons with a 2D hybrid pic-MCC model

36. Herman D et al (2012) Plasma potential and Langmuir probe measurements in the near-field plume of the NASA-300M hall thruster. In: 48th AIAA/ASME/SAE/ASEE joint propulsion conference and exhibit. https://doi.org/10.2514/6.2012-4115

37. Nakles M et al (2007) Experimental and numerical examination of the BHT-200 hall thruster plume. In: 43rd AIAA/ASME/SAE/ASEE joint propulsion conference and exhibit. https://doi.org/10.2514/6.2007-5305

38. Raitses Y, Staack D, Keidar M, Fisch N (2005) Electron-Wall interaction in hall thrusters. Phys Plasmas 12(5):Paper 057104. https://doi.org/10.1063/1.1891747

39. Duan P et al (2016) Effect of the discharge voltage on the performance of the hall thruster. Plasma Sci Technol 18(4):382–387. https://doi.org/10.1088/1009-0630/18/4/09

40. Huddleston RH, Leonard SL (1965) Plasma diagnostic techniques. Academic Press, New York

41. Lopez Ortega A et al (2015) Self-consistent model of a high-power hall thruster plume. IEEE Trans Plasma Sci 43(9):2875–2886. https://doi.org/10.1109/tps.2015.2446411

42. Taccogna F et al (2002) Particle-in-cell with Monte Carlo simulation of SPT-100 exhaust plumes. J Spacecr Rocket 39(3):409–419. https://doi.org/10.2514/2.3840

43. Fife J, Martinez-Sanchez M, Szabo J, Fife J, Martinez-Sanchez M, Szabo J (1997) A numerical study of low-frequency discharge oscillations in hall thrusters. In: Presented at the 33rd joint propulsion conference and exhibit, Seattle, WA, U.S.A

44. Dale ET, Jorns BA (2018) Non-invasive characterization of the ionization region of a hall effect thruster. In: Presented at the 2018 joint propulsion conference, Cincinnati, Ohio

45. Lobbia RB (2010) A Time-resolved Investigation of the Hall Thruster Breathing Mode. Ph.D. Thesis, The University of Michigan.

46. Fife, J. M., "Hybrid-pic modeling and electrostatic probe survey of hall thrusters," Ph.D. Thesis, Aeronautics and Astronautics, Massachusetts Institute of Technology, Cambridge, MA, 1998

Publisher's Note